Materials and Design 194 (2020) 108874

Contents lists available at ScienceDirect

Materials and Design

journal homepage: www.elsevier.com/locate/matdes

Effect of microstructural anisotropy on severe plastic deformation during material removal at micrometer length-scales

Shan Gong, M. Ravi Shankar *

Department of Industrial Engineering, University of Pittsburgh, 1048, Benedum Hall, 3700 O'Hara Street, Pittsburgh, PA 15213, USA

HIGHLIGHTS

- The homogeneity of severe plastic deformation at micrometer length-scales is orientation-dependent.
- The deformed structure from large shear strains spans from ultrafine grains to that entirely unrefined.
- The orientation of the loading determines the kinetics of dislocation annihilation and the resulting microstructure.
- Ductile fracture due to shear inhomogeneity across grain boundaries limits the integrity of inherited surfaces.
- Fundamental limits emerge on the suitability of technologies such as diamond turning in fabricating optical components.

GRAPHICAL ABSTRACT

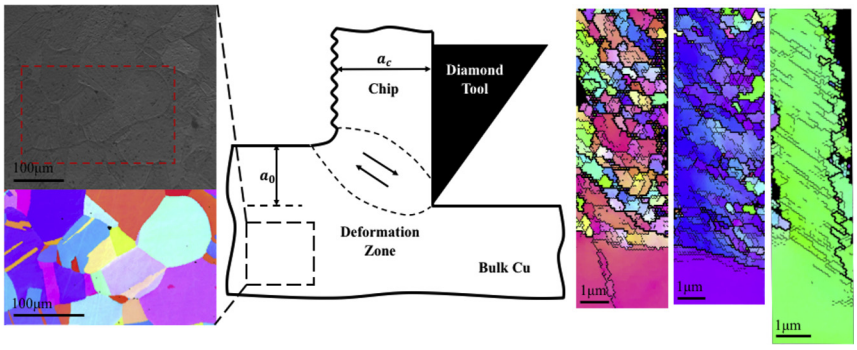

ARTICLE INFO

Article history:
Received 23 January 2020
Received in revised form 5 June 2020
Accepted 7 June 2020
Available online 08 June 2020

Keywords:
Severe plastic deformation (SPD)
Anisotropy
Deformation structure
Electron microscopy
Surface integrity

ABSTRACT

The emergence of shear inhomogeneity across grain boundaries during severe shear deformation in Cu at the micrometer length-scales is demonstrated through in situ imaging inside a scanning electron microscope. The deformation mechanics during machining is found to be orientation dependent. Microstructure refinement from severe plastic deformation in confined volumes is entirely suppressed in certain orientations but results in a characteristic ultrafine structure in others. Rampant ductile fracture is found to nucleate at some grain boundaries due to elevated dislocation densities, and this failure mechanism is imprinted on the freshly generated surface, which limits the precision of machining-based processes (e.g., diamond turning) in nanometrically-smooth roughness profiles.

1. Introduction

Plastic deformation of crystalline metals is accommodated via dislocation multiplication, annihilation, rearrangement, and (possible) twinning [1,2]. Motion of dislocations is confined to slip systems, of which mobility and glide are fundamentally determined by the lattice structure and in turn, determines the mechanical response [3]. In face-centered cubic (FCC) copper, there are 12 independent slip systems available. A slip system is activated when the applied stress τ is larger than its corresponding critical resolved shear stress τ_{CRSS}. The resolved stress components on each slip system are determined by the alignment of crystal lattice with respect to external loading. Thus, the abundance of slip systems doesn't necessitate isotropy. As for plastic deformation

* Corresponding author.
E-mail address: ravishm@pitt.edu (M.R. Shankar).

https://doi.org/10.1016/j.matdes.2020.108874

with low to moderate strain values (typically <1), only a limited number of slip systems are involved which can be predicted by Schmid factor analysis and also has been experimentally observed in uniaxial tension/compression [4,5], nanoindentation [6,7], etc. However, as strain increases into severe plastic deformation (SPD), prolific cross-slip complicates the situation. Correspondingly, investigation of microstructural evolution shows characteristic refinement of bulk grain, resulting in ultra-fine grained structures in deformed materials due to strong dislocation interactions [8,9]. Formation of dislocation tangles transform into cells and subgrain boundaries evolving with strains [10]. Furthermore, SPD often involves dynamic recovery and recrystallization (DRX) which also complicates final microstructure [11,12]. The evolvement of microstructure during plastic deformation results from both storage and annihilation/recovery of dislocations. It has been recognized that the evolution of dislocations is dependent on the crystal orientation, even in FCC materials [13]. This underpins the evolution of the hardening rate that is perceived in the flow stress and the evolution of dislocation cell structures (including cell sizes and/or misorientation across neighbors) during Stage II were found to be orientation-dependent [14–16].

Here, we purpose plane-strain machining to impose SPD in Cu at the micrometer length-scales to examine the orientation-dependent mechanics and microstructure refinement. The experimental configuration is designed to subject individual grains to SPD, one orientation at a time with the deformation depth being held much smaller than the bulk grain size. However, examining the progression of the deformation across these individual grains reveals the role of intra- and intergranular inhomogeneity on the mechanics and microstructure evolution. The deformation zone is characterized via digital image correlation (DIC) of secondary electron images. Electron backscattered diffraction (EBSD) across the deformation zone is used to reveal the microstructural consequences as a function of the parent grain structure. Meanwhile, the topographical integrity of machining surface is inherited from the modification of the deformation zone and subsequent microstructure evolution due to various alignments of bulk orientations with respect to machining tool. This is used to reveal the mechanism behind the nucleation of surface defects, which limits the precision achievable with micrometer-scale removal process (e.g., diamond turning).

2. Experimental methods

A customized sub-stage (as shown in Fig. 1a) has been built to perform deformation experiments, where the workpiece is advanced against a wedge-shaped diamond tool. This configuration is essentially one of plane-strain machining. The scale of deformation is defined by a single parameter, preset depth of cut h for a given displacement speed. This stage can fit in the vacuum chamber of Thermo Scientific™ Apreo scanning electron microscope (SEM). Since the cutting tool is kept stationary with respect to electron beam during in situ deformation experiments, the material flow from undeformed bulk through deformation zone to severely sheared chip can be monitored continuously via secondary electron (SE) imaging. In this research work, the cutting tool is a single crystal diamond with radius of edge <25 nm and the roughness (surface arithmetical mean height) of the rake plane is ~12 nm as measured from Bruker Optical Profilometer. The rake angle α is set at 0° and the clearance angle is 10°. As for other deformation parameters, the speed in advancing workpiece, V_c, was kept at a constant value of 150 μm/s and preset depth of cut h was varied from 1 μm to 3 μm.

Bulk material examined here, Oxygen-Free High Conductivity (OFHC) copper sheet (with purity of 99.99%) was annealed at 700 °C for 2 h and cut via a diamond saw into pieces of 10 mm×10 mm. To reveal the bulk microstructure, the workpiece was polished using standard metallographic preparation procedure (through 9 μm, 6 μm, 3 μm, 1 μm) down to a final step with 0.04 μm colloidal silica suspension on Struers Tegramin 25. Although the resultant mirror-like surface from polishing could yield orientation imaging microscopy (OIM) with high quality via EBSD, it lacks enough contrast for identification of individual grains in SE imaging. Thus, freshly polished surface was subsequently etched by mixture of acetic and nitric acid (with volume ratio 1:1) for around 20 s. As shown in Fig. 1b, chemical etching provides a unique sign to identify the grain being deformed when referring to crystal orientation map from EBSD. Also, the average grain size of bulk Cu is about ~100 μm ± 20 μm. In this work, grains with size >10h are selected for experiments and subsequent analysis. When comparing it with the preset depth of cut, this deformation configuration samples only a small fraction of a single grain in each increment of time (when viewing along x-axis) as shown in the SE image of Fig. 1c, i.e., intragranular deformation.

The quantitative analysis of material flow through the deformation zone was achieved via digital image correlation (DIC) [17,18]. As pointed out earlier, a sequence of SE images of the "stationary" deformation zone was recorded during in situ deformation experiments. The asperities on the surface from chemical etching offers substantial contrast for feature tracking in image correlation algorithm to characterize the material flow. For a given asperity $\boldsymbol{P} = (x,y)$ in ith image, its corresponding position in $(i+1)$th image is estimated by calculating the maximum value in two-dimensional discrete cross correlation function

$$\Phi_i(x,y) = \sum_{i=1}^{p}\sum_{j=1}^{q} f_i(x,y) \times f_i(x+m, x+n) \tag{1}$$

where $f(x,y)$ is the intensity at asperity (x,y) in the image. The displacement field $\boldsymbol{D}$ can be constructed via running the above calculation for all detecting points, which contains two components, one due to workpiece movement (rigid body motion) and the other related to shear deformation . Subsequently, the strain rate tensor is given by taking spatial and temporal differentiation of the displacement field:

$$\frac{\partial \boldsymbol{D}_p}{\partial s \partial t} = \left[\frac{\partial^2 u_p}{\partial x \partial t}\frac{1}{2}\left(\frac{\partial^2 u_p}{\partial y \partial t} + \frac{\partial^2 v_p}{\partial x \partial t}\right)\frac{1}{2}\left(\frac{\partial^2 v_p}{\partial x \partial t} + \frac{\partial^2 u_p}{\partial y \partial t}\right)\frac{\partial^2 v_p}{\partial y \partial t}\right] \tag{2}$$

In this work, the effective strain rate tensor was calculated by (taking the square root of inner product)

$$\varepsilon_p = \sqrt{\frac{2}{3}\left\langle \frac{\partial \boldsymbol{D}_p}{\partial s \partial t}, \frac{\partial \boldsymbol{D}_p}{\partial s \partial t} \right\rangle}$$

Implementation of DIC was done by MATLAB® (see Ref. [17]) and the spatial resolution (distance between two adjacent detecting points in the algorithm) is ~0.25 μm.

Specimens with partially detached chips contain full trajectory of microstructure evolution from bulk crystal to severely sheared material. These specimens were mounted with epoxy and mechanically polished using the same recipe as described earlier. The crystal orientation map was obtained by EBSD and subsequent analyses were performed by TSL OIM 7.0 and MATLAB® via MTEX [19]. In the following content, grain boundaries (GBs, without specification) and high angle boundaries (HABs) refer to boundaries with misorientations >15° while low angle boundaries (LABs) correspond to misorientations between 2° and 15°. The average grain size is the weighted mean of area separated by GBs. This value is represented as the diameter of a circle with its area equal to that for the weighted mean area of calculated grains.

3. Results and discussion

3.1. Deformation mechanics

While performing machining, choosing h much smaller (by orders-of-magnitude) than the thickness of Cu workpiece (typically ≥100 μm for all workpieces used in this work) ensures plane strain condition in

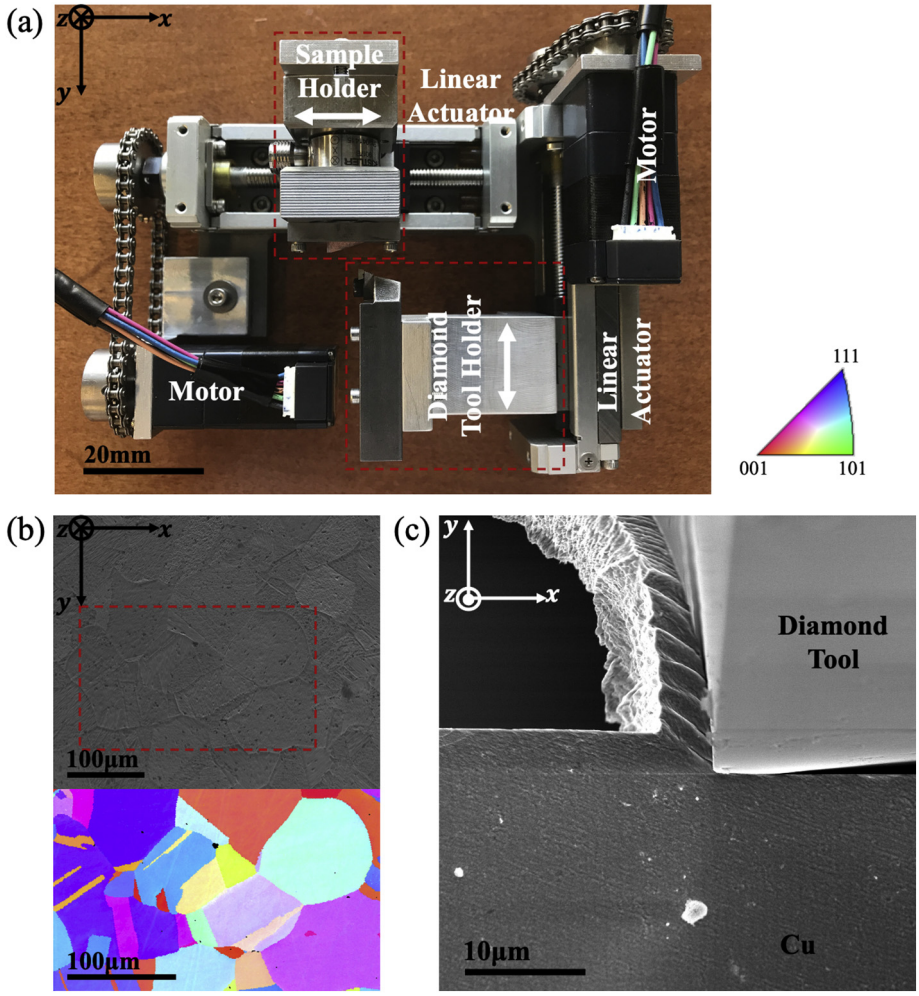

Fig. 1. (a) Customized sub-stage to perform in situ machining inside the vacuum chamber of SEM. (b) SE image of etched OFHC Cu surface and crystal orientation map obtained from EBSD corresponding to the selected area, where individual grains are readily visible due to chemical etching and their orientations can also be identified. (c) SE image of diamond tool moving across a single large grain captured during in situ experiment. Note the separation of the length-scales characterizing the bulk grain structure versus that for deformation. Essentially, one grain at a time is sampled, until a grain boundary is traversed when viewing along *x*-axis. In our experiments, the sub-stage has been tilted around *x*-axis to a few degrees (<5°) to avoid the shadowing effect from the diamond tool on the etched surface.

the deformation zone as shown in Fig. 2a. This thickness is defined normal to the *x*-*y* plane in Fig. 1c. The rake angle γ_n was kept at a constant of 0°. Thus, the corresponding effective strain imposed can be calculated via [20]:

$$\varepsilon_{eff} = \frac{\cos\gamma_n}{\sqrt{3}\,\sin\varphi\,\cos(\varphi-\alpha)} = \frac{1}{\sqrt{3}\,\sin\varphi\,\cos\varphi} \tag{3}$$

where φ (the angle between ideal shear plane and *x*-*z* plane in Fig. 2a) is determined by the ratio of preset depth of cut and thickness of deformed chip, $\tan\varphi = h/h_c$. This value was directly measured from scanning electron micrographs of partially detached chip. At the micrometer length-scale, this ratio is primarily dominated by crystal orientation being deformed for given condition as in Fig. 2b. The variation of strain values imposed on grains of different orientations is shown in Fig. 2c. For a given cutting speed V_c, the chip speed V_{ch} (Fig. 2d) and shear speed V_{sh} (Fig. 2e) can be calculated as.

$$V_{ch} = V_c\frac{\sin\varphi}{\cos(\varphi-\gamma_n)} \text{ and } V_{sh} = V_c\frac{\cos\gamma_n}{\cos(\varphi-\gamma_n)} \tag{4}$$

It can be seen that the shear speed doesn't vary a lot with crystal orientations. Note that the grain orientations in the inverse pole figure in Fig. 2b–e are defined with respect to normal direction of Cu workpiece, i.e. *z*-axis in Fig. 2a. While the deformation conditions are identical, $h =$ 1 or 2 μm and $V_c = 150$ μm/s, the material flow from severe shear is markedly divergent as a function of bulk grain orientations.

Fig. 3 shows the results of characterization of material flow through deformation zone during in situ deformation experiments via DIC. Snapshots of deformation zone corresponding to two individual grains are shown in Fig. 3a and c, of which orientations with respect to tool advancing direction are illustrated by the *insets*. Subsequently, strain-rate fields in Fig. 3b and d, were obtained by performing spatial and temporal differentiation of displacement field across deformation zone. This highly localized strain-rate field coincides with the assumption that SPD is imposed in confined zones; i.e. a nominal shear plane.

3.2. Microstructure evolution across the deformation zone

The trajectory of microstructure evolution from bulk crystal to severely deformed chip across deformation zone is retained in specimen with partially detached chip. The history of deformation from the undeformed bulk through the confined zone of deformation, where the large shear strains are accumulated can be tracked. Fig. 4 reveals the corresponding mechanics, which was obtained by deforming annealed Cu with $h = 2$ μm and $V_c = 150$ μm/s. The deformed chip essentially samples a small volume from intragranular deformation within a single crystal. In Fig. 4a, the black arrow line indicates a path with increasing strain from 0 to maximum value of ~1.5 (in this particular case). The

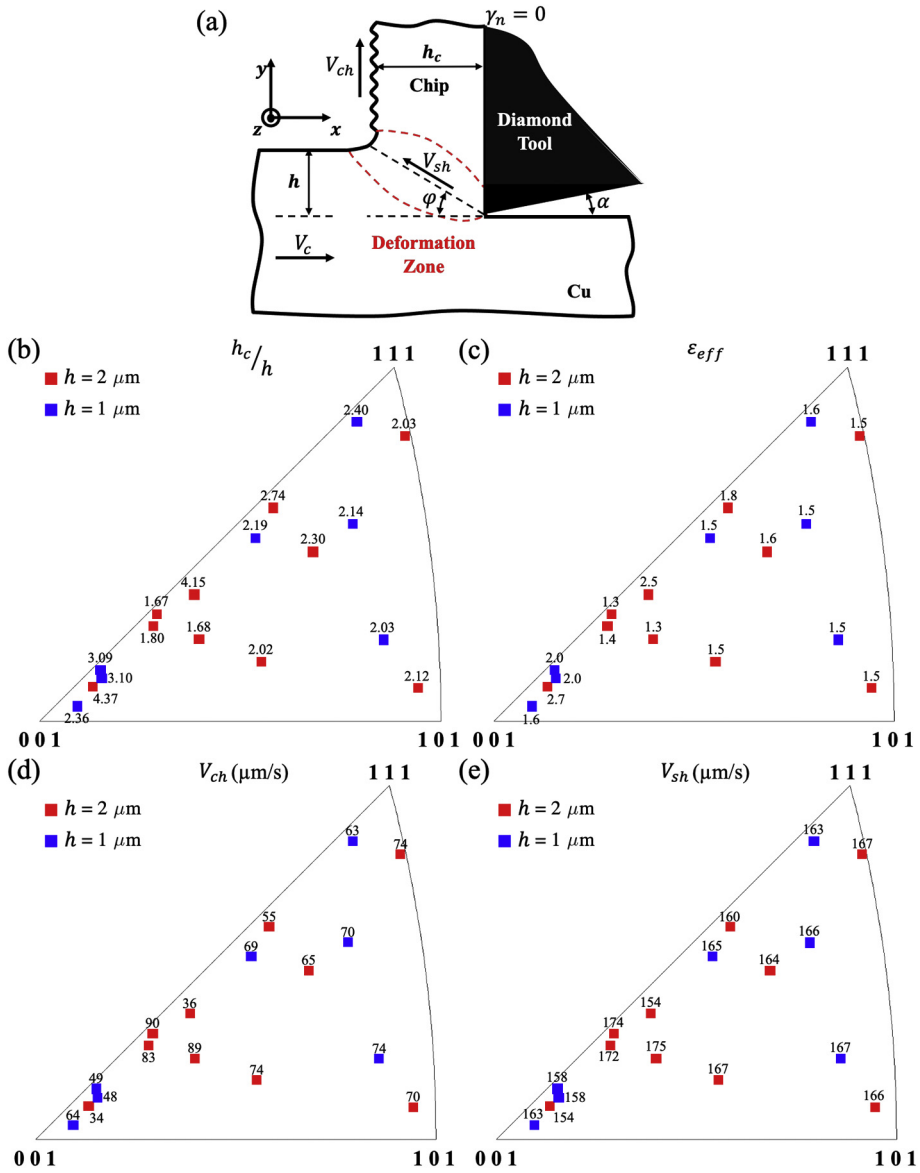

Fig. 2. (a) A schematic representation of plane strain deformation. The inverse pole figures showing the orientations of bulk grain orientations (with respect to *z*-axis) labeled with: (b) calculated chip ratio, (c) effective strain value, (d) chip speed and (e) shear speed. Loading direction with respect to the crystallographic axis influences the magnitude of plastic strain. However, all these values are within the realm of severe plastic deformation with values in excess of 1. Still, divergent pathways of microstructural evolution are shown to result, subsequently.

dislocation density in the deformation zone increases with accumulated strains, and subsequently, multiplication and rearrangement of dislocations result in formations of dislocation sub-structures including incidental dislocation boundaries (IDBs, from statistically trapped dislocations) and geometrically necessary boundaries (GNBs, because of strain gradients) [21]. The misorientations of these boundaries increase with increasing levels of strains. This is shown in Fig. 4a and d, where a HAB was found in the path from bulk grain to deformed chip. Furthermore, the aforementioned mechanism is also assisted by dynamic recrystallization (DRX), which is mainly responsible for the "dislocation-free" (or low density) regions surrounded by HABs in the deformed chips as can be seen in the kernel average misorientation map in Fig. 4b.

3.3. Microstructure in deformed chips

The microstructure of the deformed chip shown in Fig. 4a is anomalous in comparison to conventional expectation that severe plastic deformation results in ultra-fine grain structures. It is clear from Fig. 5 that some orientations follow the expected trajectory of microstructure refinement in response to large strains, while others do not. The microstructural refinement, at least at the deformation scales examined here ($h = 2$ μm and $V_c = 150$ μm/s), are markedly orientation dependent.

It is important to distinguish this behavior from confounding thermal effects. The machining is a thermo-mechanically coupled deformation system where corresponding microstructure evolution can be altered by temperature rise [22]. It is difficult to perform direct thermometry on the deformation zone during in situ experiments in SEM. The deformation conditions (small preset depth of cut and also low cutting speed) were chosen to preclude any significant bulk heating of the chips. Thus, the microstructural refinement is likely due to suppressed storage of dislocations. Note, that the strain values across the orientations of loading are in excess of an effective strain of 1. Despite this, some of the orientations show a distinct lack of refinement as illustrated in Fig. 5d. It has been pointed out by Kocks and Mecking [13], the evolution of dislocation density with incremental strain is given by

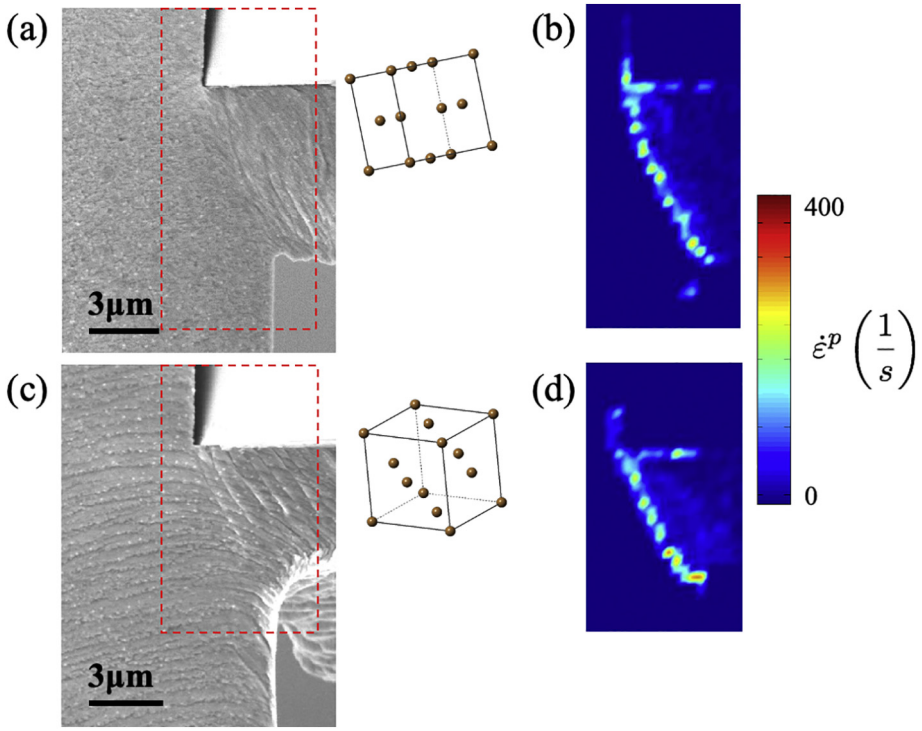

Fig. 3. SE images of the deformation zone for performing DIC captured during in situ experiment with $h = 3$ μm and $V_c = 150$ μm/s of two grains (a) and (c), with *insets* illustrating crystal lattice with respect to the direction of tool advancing. (b) and (d) Strain rate fields obtained from DIC corresponding to the areas outlined by dash-lined rectangles in (a) and (c) respectively.

$$\frac{d\rho}{d\varepsilon} = \frac{1}{b}\left(k_1\sqrt{\rho_s} - k_2\rho_s\right) \tag{5}$$

where the first term accounts for the rate at which the mobile dislocations are stored and the second term $k_2\rho_s$ represents the annihilation rate corresponding to dynamic recovery. The dynamic recovery occurs in process, during the imposition of the large strains. Given the fact the deformation zone is strongly non-homogenous, a high strain gradient is embedded. Its presence necessitates the generation of geometrically necessary dislocations (GNDs), which are required to maintain the deformation compatibility. Thus, another component shall be taken into account:

$$\frac{d\rho}{d\varepsilon} = \frac{1}{b}\left(k_1\sqrt{\rho_s} - k_2\rho_s + k_3\rho_g\right) \tag{6}$$

where the third term $k_3\rho_g$ represents the contribution from GNDs. The density of GNDs, ρ_g is proportional to the strain gradient [23].

A transition in the work hardening behavior with increasing levels of strain is the decline in the hardening rate with the onset of the so-called Stage III deformation. The onset of Stage III deformation is determined by a characteristic critical stress τ_{III}, which depends on the crystal orientation at room temperature. Kubin [24] assumed that dynamic recovery occurs by cross-slip and annihilation where two screw dislocations of opposite signs cancel each other. The rate of annihilation is defined by a critical annihilation distance of screw dislocations y^{hkl} (here the superscript hkl refers to the crystal orientation) which follows $y^{hkl}\tau_{III}^{hkl} \propto C\mu b$ (where C is a constant, and μ is the shear modulus) [24]. So, a small value of τ_{III} will yield a large critical annihilation distance, which means two screw dislocations of opposite signs can annihilate over a large distance. The determination of τ_{III} typically comes from uniaxial tension/compression tests, referring to the resolved shear stress on the primary slip plane. Subsequently, the variation in τ_{III} with respect to orientation refers to the change in loading direction (equivalent to crystal orientation when viewing along loading direction) [25].

As shown in Fig. 5a and b, the material undergoes shear deformation in both uniaxial tension and machining of single crystals. We realize that the strain levels examined in this study far outstrip the Stage III behavior examined in tension tests. However, to draw parallels, we rotated the orientations that were observed with respect to (w.r.t.) the z-axis as shown in Fig. 2 to along the cutting direction. Thus, we are able to draw a one-to-one correspondence between our experiments and those considered earlier [25] in Fig. 5a, which shows the τ_{III} values as a function of tensile loading direction. Fig. 5b illustrates the microstructure characteristics (refinement or lack of refinement) in deformed chips with respect to tool loading orientation. For deformed chips with characteristic grain refinement (one is shown in Fig. 5c), it was found that the average grain size in deformed chips is in the range of 150 nm to 350 nm for crystals examined in this work, which is generally smaller than a quarter of preset depth of cut h used. Here, a working definition for aforementioned "lack of refinement" is proposed as the average grain size in deformed chips is larger than 50% of present depth of cut, i.e. . When comparing Fig. 5a and b, we find that the crystal orientations which feature lack of refinement after severe shear deformation are close to the orientations that feature a low τ_{III}^{hkl}. A low τ_{III}^{hkl} means a large critical annihilation length y_{III}^{hkl} which leads to enhanced dynamic recovery. Rampant annihilation in confined volumes that were subjected to large shear deformation subsequently resulted in coarser dislocation sub-structures. The progressive evolution and refinement of substructures underpins the typical ultra-fine microstructure. Magnified dynamic recovery in certain orientations appears to preempt such refinement. The lack in dislocation density necessitates the decrease in formation of dislocation substructures and subsequently the reorientation is also suppressed across a confined deformation volume as Fig. 5d in contrast to the conventional ultra-fine microstructure in Fig. 5c.

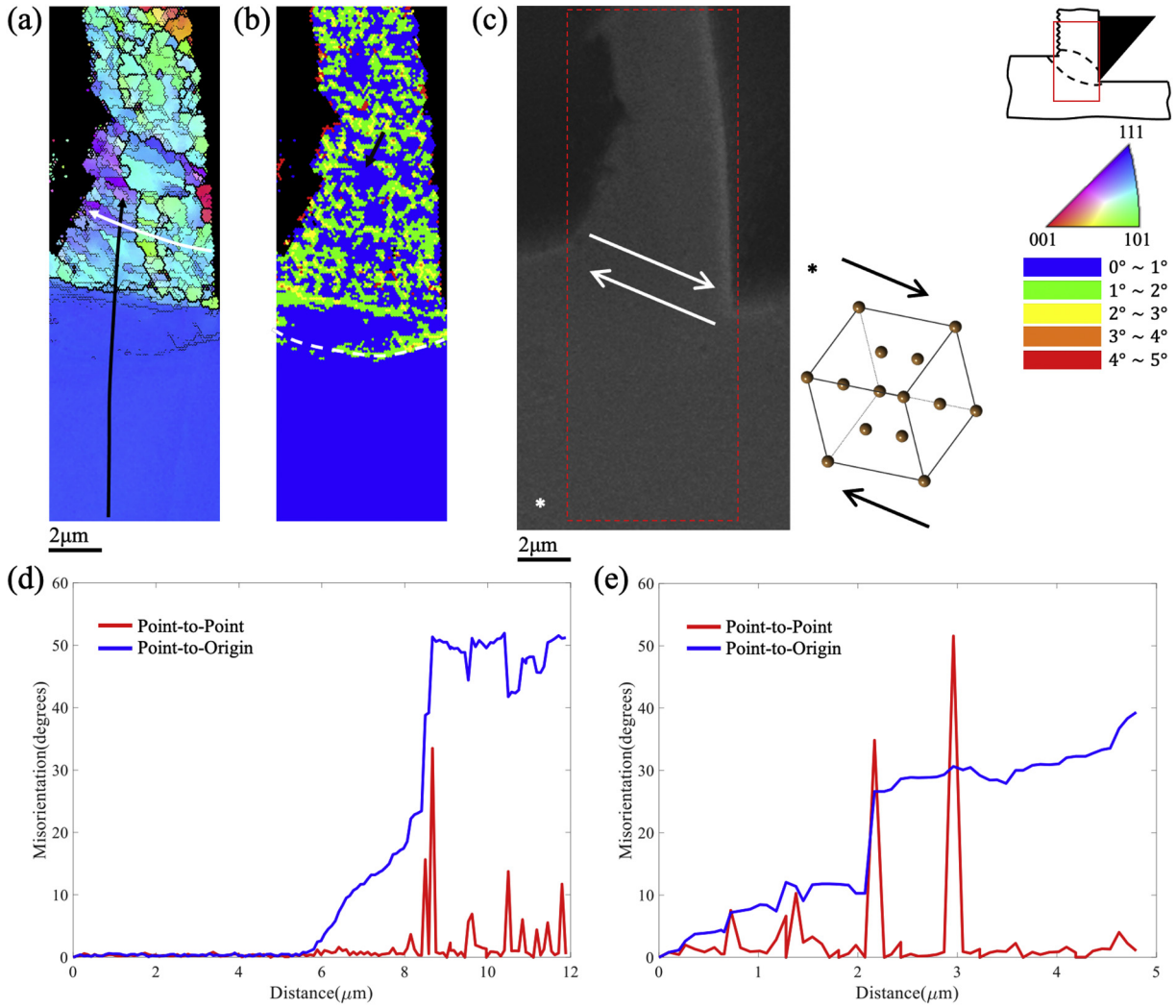

Fig. 4. (a) Crystal orientation map and (b) corresponding kernel average misorientation map of a partially detached chip to illustrate the microstructure evolution. (c) SE image of specimen with partially detached chip with rectangles indicating the location of EBSD, with *insets* illustrating crystal lattice with respect to the direction of tool advancing. The nominal shear direction is illustrated by two white arrows. Misorientation maps (d) along the path by black arrow and (e) by white arrow calculated from (a). In the crystal orientation map: boundaries with misorientation larger than 15° are represented by thicker lines and those with misorientation between 2° and 15° by thinner lines. Refer to the red rectangle in the schematic for the location where EBSD was performed.

3.4. Deformation transition across grain boundary

It is inevitable to encounter grain boundaries as deformation continues given the polycrystalline nature of workpiece. The in situ characterization of material flow across grain boundary is shown in Fig. 6. Fig. 6a demonstrates an ideal case of deformation transition. As diamond tool approached grain boundary (illustrated by the white line in Fig. 6a), the deformation in grain *B* was readily initiated once the deformation zone extended across the boundary as indicated by the white arrow. Severe plastic deformation was transmitted from grain *A* to *B* without any noticeable incompatibility. The anisotropy in deformation behavior is nonetheless apparent, which is characteristic of the bulk grain orientation. In this particular case, the deformed chip from grain *B* demonstrates a more saw-toothed geometry that is clearly morphologically distinct from that of grain *A*. *A* deforms homogeneously, via continuous simple shear. (Refer to Fig. 1c, the chip remains an integral, contiguous without any observable cracking; the observed lamellar features are merely topographical.) But this transition appears to be smooth and there does not appear to be any instability or incompatibility during the transition.

This transition, however, is not always the norm. As shown in Fig. 6b, there was no sign of activation of shear deformation in grain *D* even though the diamond tool was advanced right up to the grain boundary, leading to a formation of notch in the deformed chip as shown in Fig. 6b-9. Note that imaging artifacts and contrast changes at sharp corners of insulating materials often shown up in secondary electron images which cause the difference in the appearance of diamond tool in Fig. 6a and b. We should be careful to not to read too much into them. During plastic deformation, grain boundaries potentially act as obstacles to dislocation motion. In the configuration imposed by plane strain deformation as shown in Fig. 6b, dislocations will inevitably accumulate near the grain boundary as the diamond tool approaches. The localized dislocation pile-ups lead to an increase in vacancy concentration [26]. Those vacancies tend to gather around deformation-induced boundaries, and such condensation results in voids formation. Subsequently, voids grow through consumption of dislocations [27]. This enhanced voids generation and coalescence result in the occurrence of ductile tearing in the vicinity of grain boundary as shown in Fig. 7. Ductile tearing in this manner induces an instability in the plastic deformation and the mechanics of surface generation. This holds implications for the

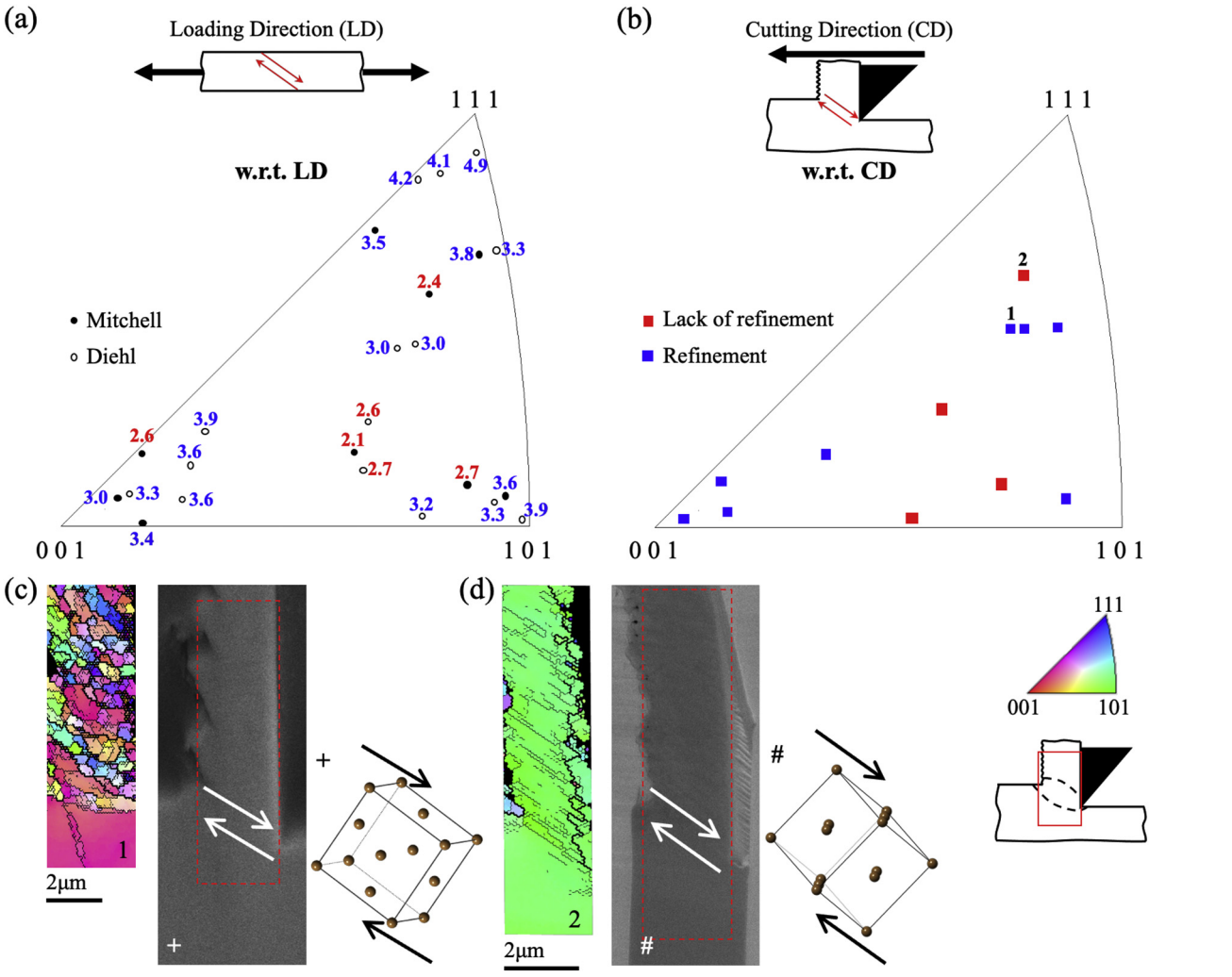

Fig. 5. (a) τ_{III} (kg/mm^2) of Cu with respect to crystal orientation (after Mitchell and Diehl [25]). (b) Summary of microstructure characteristics (refinement or lack of refinement) with respect to cutting direction. Crystal orientation maps from EBSD of deformed chips from two different bulk grains (c) and (d) with identical deforming conditions $h = 2$ μm and $V_c = 150$ μm/s. (*Inset*) in (c) and (d) SE images of specimen with partially detached chip with rectangle indicating the location of EBSD, with crystal lattice illustrating the direction of tool advancing. The nominal shear direction is illustrated by two arrows. Resolving the principal shear direction as a function of crystallographic orientation reveals a correspondence with trends in dynamic recovery in tension tests. Our comparison is based on relating principal shear direction in our experiments versus that in tension.

integrity of the surfaces that are generated via micrometer-scale machining operations, which is critical to the fabrication of diamond-turned optics and superfinished surfaces.

3.5. Surface integrity

Formation of deformed chips and generation of underlying surface are tightly interrelated. The aforementioned anisotropic material response to severe plastic deformation imposed by machining not only results in morphological and microstructural variation in deformed chips but also the surface integrity especially in the vicinity of grain boundary. Not surprisingly, the surface from a smooth deformation transition across grain boundary as in Fig. 6a didn't reveal any topographical change along the grain boundary as in Fig. 8a. Meanwhile, the aforementioned ductile tearing is imprinted on the surface resulting in grain boundary defect (i.e., abrupt roughness changes across boundary) as captured in Fig. 8b. We note that this defect is not related to the material side flow as this defect extends along the whole grain boundary. Furthermore, it also appears in the region away from the edge as shown in Fig. 8d and e. This failure mechanism essentially limits the precision of surface in diamond-turning process. Note that the cutting-edge topography is also imprinted on the surface after machining which corresponds to the longitudinal scratches across the whole region as shown in Fig. 8. This tooling-mark due to the imperfection of the cutting edge shall be distinguished from the aforementioned grain boundary defect which is inherited from microstructural effects. Noell [28] pointed out that deformation-induced boundaries are sites for voids generation. Although vacancies formation increases with increasing dislocation density, the formation of voids via vacancy coalescence is a stochastic process. Thus, the two boundaries in Fig. 6 exert different effects on the surface integrity. With aid of in situ experiment, the source of topographical defects inherited by the freshly generated surfaces becomes apparent. Instabilities in plastic flow across grain boundaries lead to deterioration of surface finish in precision machining processes.

4. Conclusions

The effect of bulk grain orientation on severe plastic deformation imposed by machining on annealed OFHC Cu with preset depth of cut $h <$ 3 μm was examined. The effect of cutting orientation with respect to the crystal axis revealed an anisotropic response to both the mechanics of plasticity and the resulting microstructure evolution. With aid of in situ experiments, the deformation mechanics were examined via DIC. The deformation zone was characteristically confined to sub-

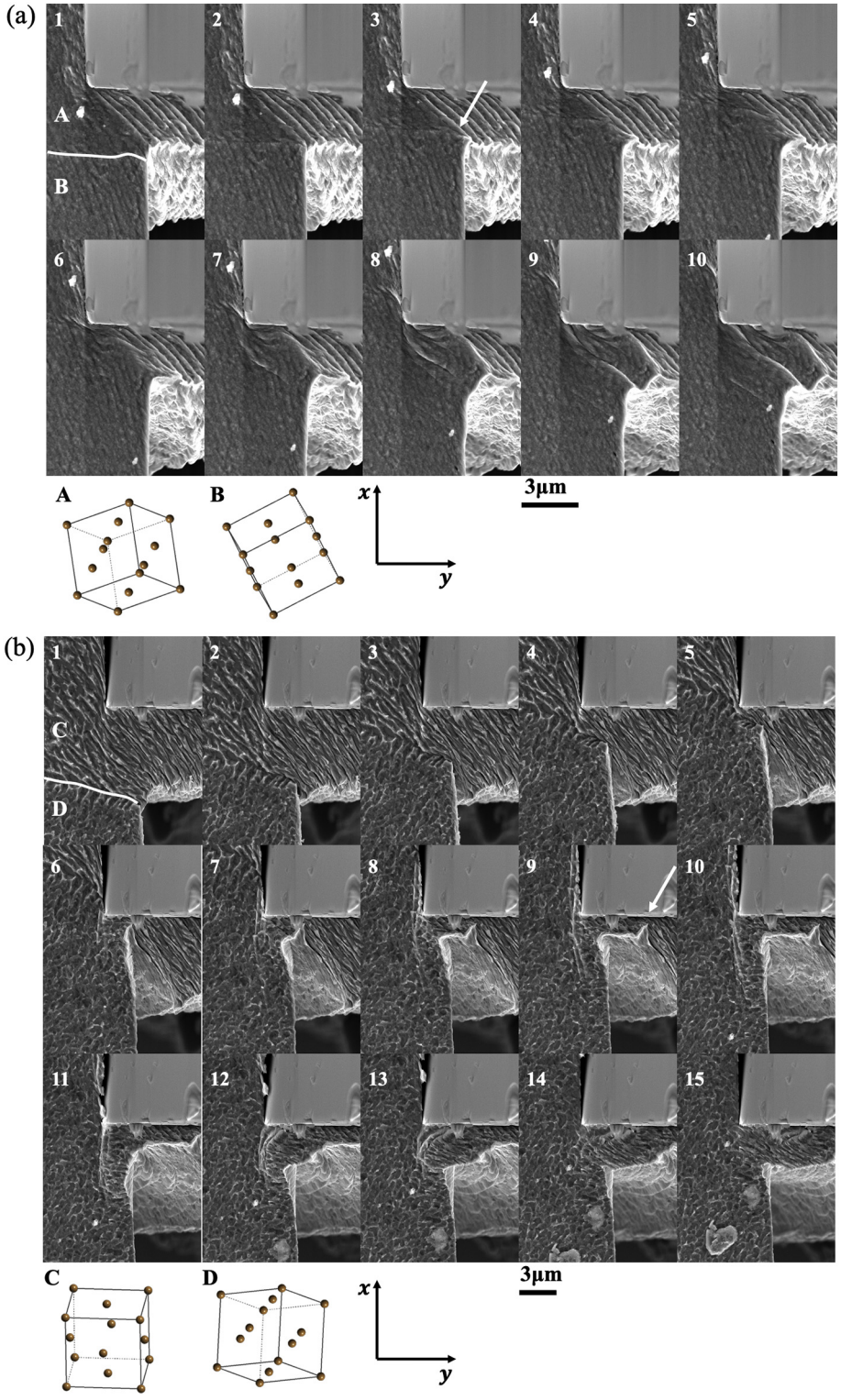

Fig. 6. Sequence of SE images of the deformation zone in annealed OFHC Cu when diamond tool moves across grain boundaries (illustrated by white line in the image) in two distinct cases (a) and (b), also see Supplementary Movies 1 and 2. (*Inset*) illustration of crystal lattices. Deformation condition: $h = 3$ μm and $V_c = 150$ μm/s.

micrometer length-scales, but manifested differing levels of shear strain as a function of orientation–all else held identical. The microstructure evolution during severe plastic deformation was characterized by performing EBSD, which revealed behavior ranging from the expected refinement to complete lack thereof. This variation in microstructural response is attributed to the anisotropic accumulation of dislocations as a function of the loading direction. We find striking parallels to the observed anisotropy in the dynamic recovery behavior as a function of the orientation in uniaxial loading. The mechanics of deformation that leads to the chip formation also holds implications for the integrity of the

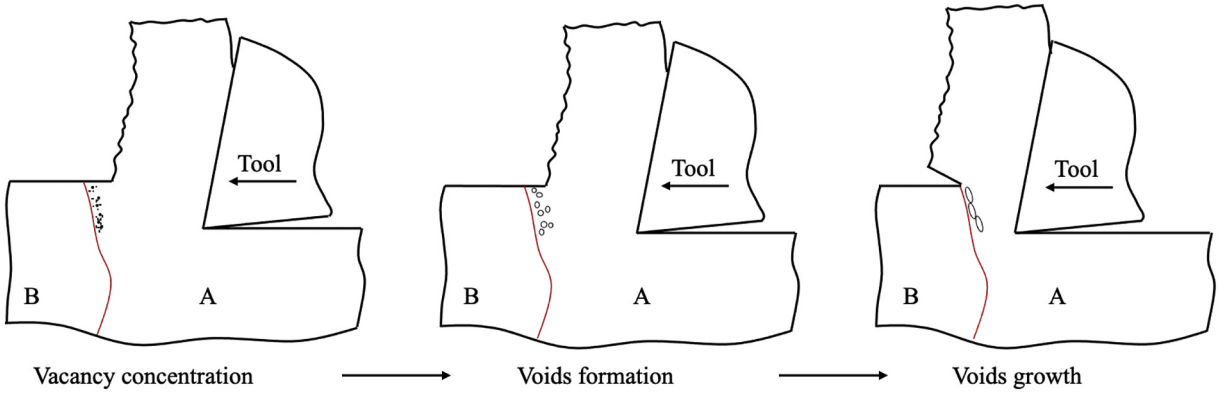

Fig. 7. Illustration of ductile tearing as diamond tool approaches grain boundary.

freshly generated surfaces. The switch-over in the mechanics of strain accommodation leads to ductile tearing at grain boundaries. These instabilities are inherited by the surface, which limit the surface integrity that can be generated using processes, such as diamond turning.

Supplementary data to this article can be found online at https://doi.org/10.1016/j.matdes.2020.108874.

CRediT authorship contribution statement

Shan Gong: Data curation, Formal analysis, Investigation, Methodology, Writing - original draft. **M. Ravi Shankar:** Conceptualization, Formal analysis, Funding acquisition, Project administration, Resources, Supervision, Writing - review & editing.

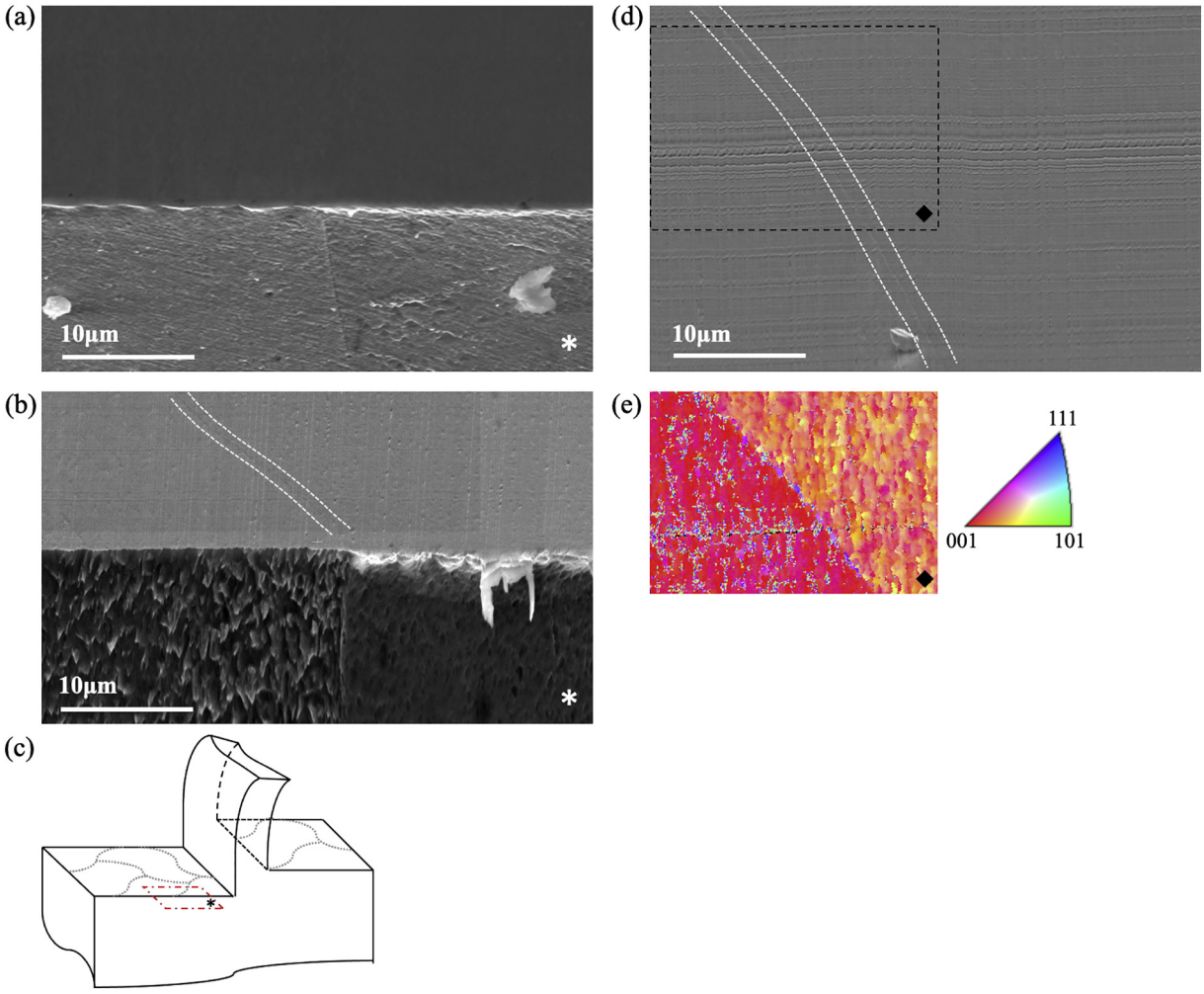

Fig. 8. SE images of the surface from machining across grain boundaries: (a) and (b) corresponding to machining process in Fig. 6(a) and (b), respectively. (c) Schematic indicating the position where SE images were taken. (d) SE image of surface with grain boundary defect under preset depth of cut $h = 1$ μm with constant velocity $V_c = 150$ μm/s. (e) Crystal orientation map obtained by EBSD corresponding to the area as indicated by the black rectangle in (d). The grain boundary defects are outlined by white dashed lines.

Declaration of competing interest

The authors declare that they have no known competing financial interests or personal relationships that could have appeared to influence the work reported in this paper.

Acknowledgement

Support from II-VI Foundation Block Gift Program and the National Science Foundation (1635966) is gratefully acknowledged. We are also grateful to each of the reviewers, who provided extensive comments, which helped to generate a significantly improved manuscript.

Data availability

The raw/processed data required to reproduce these findings cannot be shared at this time as the data also forms part of an ongoing study. The relevant data can be made available on request.

References

[1] E. Nes, Modelling of work hardening and stress saturation in FCC metals, Prog. Mater. Sci. 41 (1997) 129–193, https://doi.org/10.1016/S0079-6425(97)00032-7.
[2] S.S. Cai, X.W. Li, N.R. Tao, Orientation dependence of deformation twinning in cu single crystals, J. Mater. Sci. Technol. 34 (2018) 1364–1370, https://doi.org/10.1016/j.jmst.2017.10.004.
[3] G. Winther, X. Huang, Dislocation structures. Part II. Slip system dependence, Philos. Mag. 87 (2007) 5215–5235, https://doi.org/10.1080/14786430701591505.
[4] D.V. Lychagin, S.Y. Tarasov, A.V. Chumaevskii, E.A. Alfyorova, Macrosegmentation and strain hardening stages in copper single crystals under compression, Int. J. Plast. 69 (2015) 36–53, https://doi.org/10.1016/j.ijplas.2015.01.007.
[5] N. Wieczorek, G. Laplanche, J.K. Heyer, A.B. Parsa, J. Pfetzing-Micklich, G. Eggeler, Assessment of strain hardening in copper single crystals using in situ SEM microshear experiments, Acta Mater. 113 (2016) 320–334, https://doi.org/10.1016/j.actamat.2016.04.055.
[6] W. Zhang, Y. Gao, Y. Xia, H. Bei, Indentation Schmid factor and incipient plasticity by nanoindentation pop-in tests in hexagonal close-packed single crystals, Acta Mater. 134 (2017) 53–65, https://doi.org/10.1016/j.actamat.2017.05.058.
[7] N. Zhou, K.I. Elkhodary, X. Huang, S. Tang, Y. Li, Dislocation structure and dynamics govern pop-in modes of nanoindentation on single-crystal metals, Philos. Mag. 0 (2020) 1–22. doi:https://doi.org/10.1080/14786435.2020.1739348.
[8] A. Mishra, B.K. Kad, F. Gregori, M.A. Meyers, Microstructural evolution in copper subjected to severe plastic deformation: experiments and analysis, Acta Mater. 55 (2007) 13–28, https://doi.org/10.1016/j.actamat.2006.07.008.
[9] E. Bagherpour, F. Qods, R. Ebrahimi, H. Miyamoto, Microstructure quantification of ultrafine grained pure copper fabricated by simple shear extrusion (SSE) technique, Mater. Sci. Eng. A 674 (2016) 221–231, https://doi.org/10.1016/j.msea.2016.08.001.
[10] D.L. Holt, Dislocation cell formation in metals, J. Appl. Phys. 41 (1970) 3197–3201, https://doi.org/10.1063/1.1659399.
[11] Y. Amouyal, S.V. Divinski, L. Klinger, E. Rabkin, Grain boundary diffusion and recrystallization in ultrafine grain copper produced by equal channel angular pressing, Acta Mater. 56 (2008) 5500–5513, https://doi.org/10.1016/j.actamat.2008.07.029.
[12] J. Humphreys, G.S. Rohrer, A.D. Rollett, Recrystallization and Related Annealing Phenomena, Elsevier, 2017.
[13] U.F. Kocks, H. Mecking, Physics and phenomenology of strain hardening: the FCC case, Prog. Mater. Sci. 48 (2003) 171–273, https://doi.org/10.4324/9781315279015.
[14] P.J. Hurley, F.J. Humphreys, The application of EBSD to the study of substructural development in a cold rolled single-phase aluminium alloy, Acta Mater. 51 (2003) 1087–1102, https://doi.org/10.1016/S1359-6454(02)00513-X.
[15] A. Brahme, J. Fridy, H. Weiland, A.D. Rollett, Modeling texture evolution during recrystallization in aluminum, Model. Simul. Mater. Sci. Eng. 17 (2009)https://doi.org/10.1088/0965-0393/17/1/015005.
[16] M. Stricker, M. Sudmanns, K. Schulz, T. Hochrainer, D. Weygand, Dislocation multiplication in stage II deformation of fcc multi-slip single crystals, J. Mech. Phys. Solids. 119 (2018) 319–333, https://doi.org/10.1016/j.jmps.2018.07.003.
[17] S. Basu, M.R. Shankar, Spatial confinement-induced switchover in microstructure evolution during severe plastic deformation at micrometer length scales, Acta Mater. 79 (2014) 146–158, https://doi.org/10.1016/j.actamat.2014.07.004.
[18] S. Lee, J. Hwang, M. Ravi Shankar, S. Chandrasekar, W.D. Compton, Large strain deformation field in machining, Metall. Mater. Trans. A Phys. Metall. Mater. Sci. 37 (2006) 1633–1643, https://doi.org/10.1007/s11661-006-0105-z.
[19] R. Hielscher, H. Schaeben, A novel pole figure inversion method: specification of the MTEX algorithm, J. Appl. Crystallogr. 41 (2008) 1024–1037, https://doi.org/10.1107/S0021889808030112.
[20] M.C. Shaw, J. Cookson, Metal cutting principles, Oxford university press, New York, 2005.
[21] D.A. Hughes, N. Hansen, The microstructural origin of work hardening stages, Acta Mater. 148 (2018) 374–383, https://doi.org/10.1016/j.actamat.2018.02.002.
[22] S. Shekhar, S. Abolghasem, S. Basu, J. Cai, M.R. Shankar, Effect of severe plastic deformation in machining elucidated via rate-strain-microstructure mappings, J. Manuf. Sci. Eng. Trans. ASME. 134 (2012)https://doi.org/10.1115/1.4006549.
[23] C.F.O. Dahlberg, M. Boåsen, Evolution of the length scale in strain gradient plasticity, Int. J. Plast. 112 (2019) 220–241, https://doi.org/10.1016/j.ijplas.2018.08.016.
[24] L. Kubin, T. Hoc, B. Devincre, Dynamic recovery and its orientation dependence in face-centered cubic crystals, Acta Mater. 57 (2009) 2567–2575, https://doi.org/10.1016/j.actamat.2009.02.013.
[25] T.E. Mitchell, Dislocations and plasticity in single crystals of face-centred cubic metals and alloys, Prog. Appl. Mater. Res. 6 (1964) 117–237.
[26] M.J. Zehetbauer, G. Steiner, E. Schafler, A. Korznikov, E. Korznikova, Deformation induced vacancies with severe plastic deformation: measurements and modelling, Mater. Sci. Forum 503–504 (2006) 57–64, https://doi.org/10.4028/www.scientific.net/msf.503-504.57.
[27] G. Saada, Sur la nature des défauts ponctuels crées par le croisement des dislocations, Acta Metall. 9 (1961) 965–966.
[28] P. Noell, J. Carroll, K. Hattar, B. Clark, B. Boyce, Do voids nucleate at grain boundaries during ductile rupture? Acta Mater. 137 (2017) 103–114, https://doi.org/10.1016/j.actamat.2017.07.004.